Si-nanocrystal-based LEDs fabricated by ion implantation and plasma-enhanced chemical vapour deposition

Nanotechnology **20** (2009) 405201 (10pp) doi:10.1088/0957-4484/20/40/405201

Si-nanocrystal-based LEDs fabricated by ion implantation and plasma-enhanced chemical vapour deposition

M Perálvarez[1], J Barreto[2], Josep Carreras[1], A Morales[3], D Navarro-Urrios[1], Y Lebour[1], C Domínguez[2] and B Garrido[1]

[1] MIND, IN^{2}UB, Department of Electronics, University of Barcelona, C/Marti i Franques 1, PL2, E-08028 Barcelona, Spain
[2] IMB-CNM, CSIC, Bellaterra, E-08193 Barcelona, Spain
[3] INAOE, Electronics Department, Apartado 51, Puebla 72000, Mexico

E-mail: mperalvarez@el.ub.es

Received 10 June 2009, in final form 1 August 2009
Published 8 September 2009
Online at stacks.iop.org/Nano/20/405201

Abstract

An in-depth study of the physical and electrical properties of Si-nanocrystal-based MOSLEDs is presented. The active layers were fabricated with different concentrations of Si by both ion implantation and plasma-enhanced chemical vapour deposition.

Devices fabricated by ion implantation exhibit a combination of direct current and field-effect luminescence under a bipolar pulsed excitation. The onset of the emission decreases with the Si excess from 6 to 3 V. The direct current emission is attributed to impact ionization and is associated with the reasonably high current levels observed in current–voltage measurements. This behaviour is in good agreement with transmission electron microscopy images that revealed a continuous and uniform Si nanocrystal distribution. The emission power efficiency is relatively low, $\sim 10^{-3}\%$, and the emission intensity exhibits fast degradation rates, as revealed from accelerated ageing experiments.

Devices fabricated by chemical deposition only exhibit field-effect luminescence, whose onset decreases with the Si excess from 20 to 6 V. The absence of the continuous emission is explained by the observation of a 5 nm region free of nanocrystals, which strongly reduces the direct current through the gate. The main benefit of having this nanocrystal-free region is that tunnelling current flow assisted by nanocrystals is blocked by the SiO_2 stack so that power consumption is strongly reduced, which in return increases the device power efficiency up to 0.1%. In addition, the accelerated ageing studies reveal a 50% degradation rate reduction as compared to implanted structures.

1. Introduction

Monolithic silicon light-emitting diodes (LEDs) and lasers are expected to dramatically evolve silicon technology by opening up new areas of application for Si never thought possible in the past [1–5]. With the aim of improving the radiative recombination rate in Si, Si nanocrystals (Si-nc) have been object of extensive research since the electron and hole wavefunctions are confined into a small volume. Nowadays, systems composed of Si-nc embedded in SiO_2 (silicon dioxide) represent a promising alternative thanks to their chemical stability and tunable emission in the red–infrared range (from 1.4 to 1.7 eV).

A wide variety of techniques are used for the fabrication of Si-nc/SiO_2 layers, all of them based on first preparing silicon-rich-oxide (SRO) layers and annealling in order to propitiate the Si-nc growth. Ion implantation and plasma-enhanced chemical vapour deposition (PECVD) are two of the most frequently reported. In the former, the excess of silicon is generated by implantation of Si atoms into thermally grown oxide. This technique provides an accurate method to control the silicon profile since the Si dose and implantation energy can be precisely monitored. However, ion implantation presents two main drawbacks: (i) the impact of the incident ions on the host matrix generates an undesired concentration of defects and

Table 1. PECVD samples.

Sample	$\frac{[N_2O]}{[SiH_4]}$	$[Si]_{ex}$ (at.%)	Thickness (nm)	
			As-deposited	Annealed
P1	22.00	5.39 ± 1.64	107 ± 4	102 ± 4
P2	9.17	10.92 ± 1.41	110 ± 4	88 ± 1
P3	5.50	16.94 ± 1.37	93 ± 5	74 ± 3
P4	3.60	26.10 ± 1.38	105 ± 3	85 ± 2
P5	2.20	42.06 ± 1.33	33 ± 10	22 ± 4

(ii) the achievement of uniform Si profiles in thick oxide layers is limited by the energy required to perform deep implantation processes. By PECVD, the fabrication of thick SRO layers is possible. The plasma-enhanced process stands out against the different deposition techniques as thicker layers can be rapidly grown at low temperatures. However, as in the case of the ion implantation technique, the concentration of defects must be controlled, a process that strongly depends on the deposition rate.

In recent years, the emission from Si-nc-based materials under electrical pumping has been widely reported [6–9], mostly under DC (direct current) polarization. The application of relatively high voltages under the DC regime may compromise the reliability of the device due to the high currents involved which result in fast degradation rates. In thinner devices, this degradation can be overcome, but at the cost of its emission efficiency due to the increase of the continuous leakage current between the electrodes. Latest studies have demonstrated electroluminescence (EL) emission under alternate polarization applying the concept of field-effect luminescence [10, 11]. This mechanism, which consists of sequential injection of electrons and holes from the substrate, optimizes the device's electrical stress and reduces the power consumption, leading to higher emission efficiencies.

In this work, we establish a correlation between the structural properties of SRO layers fabricated by PECVD and ion implantation and the electrical and electro-optical properties of LEDs fabricated under similar conditions. The field-effect luminescence is studied in depth, paying special attention to the divergences observed between the structures fabricated by these two elaboration techniques.

2. Experimental details

Two sets of SRO layers were fabricated onto a p-type Si substrate (resistivity of 0.1–1.4 Ω cm) by PECVD and ion implantation with different Si excesses. Their characteristics are detailed in tables 1 for PECVD and 2 for implanted films. The samples are referred to by P for PECVD and I for ion-implanted. With respect to Si-nc fabricated by PECVD, a detailed description of the preparation process can be found in [10]. In the case of samples fabricated by ion implantation, the layers were fabricated by implantation of silicon into thermally grown silicon oxide in a two-step process (energies of 25 and 50 keV). In order to obtain a flat profile of Si throughout the active layer, a ∼30 nm thick buffer layer of Si_3N_4 (silicon nitride) was deposited by PECVD onto the oxide layer before the implantation. The results of the implantation

Table 2. Ion-implanted samples.

Sample	Dose ($\times 10^{16}$ cm^{-2})	Ion energy (keV)	$[Si]_{ex}$ (at.%)	Thickness (nm)	
				Si_3N_4	SRO
I1	0.6	25	7.45±1.68	17.0±1.0	42.4±0.8
	2.4	50			
I2	1.2	25	9.37±1.63	18.3±0.4	65.5±0.4
	4.8	50			
I3	1.8	25	11.21±1.55	20.0±4.0	60.0±3.0
	7.2	50			
I4	2.4	25	14.25±1.50	21.0±1.0	42.0±1.0
	9.6	50			

Table 3. MOS devices (PECVD).

Sample	$\frac{[N_2O]}{[SiH_4]}$	$[Si]_{ex}$ (nm)	Thickness (at.%)	C_{max} (pF)	N_t (cm^{-2})	Charged nc (%)
PD1	—	0	41.1 ± 0.3	209.83	1.654×10^9	—
PD2	13	7.9	45 ± 4	239.85	1.438×10^{10}	0.4
PD3	10	9.9	44 ± 5	248.18	3.517×10^{11}	8.9
PD4	7	13.7	48 ± 9	281.67	3.681×10^{12}	85.2
PD5	5	18.8	47 ± 6	297.24	3.835×10^{12}	90.7

process were previously simulated by SRIM (stopping and range of ions in matter) calculations [12]. The phase separation and growth of the Si-nc was achieved by subjecting the SRO layers to high temperature annealing at 1100 °C in N_2 atmosphere for 4 h.

Ellipsometry measurements were performed to evaluate the thickness and the refractive index of the different active layers using a Rudolph Research AutoEl IV ellipsometer, operating at 632.8 nm under an incidence angle of 70°. XPS (x-ray photoelectron spectroscopy) measurements were performed in order to study the composition profiles. The cross-section images of the samples and the size distribution of Si nanocrystals were obtained by EFTEM (energy-filtered transmission electron microscopy). Photoluminescence (PL) spectra were measured by exciting the samples with an He–Cd laser at 325 nm. The detection set-up was composed of a 0.6 m monochromator and a GaAs photomultiplier for measurements in the visible. Time-resolved PL was measured by pumping with an Ar^+ operating at 488 nm. The optical excitation was modulated with a Brimrose FQM-80-2 acousto-optic modulator with ∼0.195 μs characteristic rise time. The emission transients were detected with a photon-counting set-up composed of a Hamamatsu thermoelectrically cooled H7422-50 photomultiplier and a Stanford Research SR430 multi-channel scaler/averager.

In the next stage, Si-nc-based metal oxide semiconductor (MOS) structures were fabricated and characterized. Tables 3 and 4 show some experimental data of PECVD and implanted devices, respectively. PECVD devices are labelled as PD and implanted ones are labelled as ID. Note that, in this case, the fabrication parameters are slightly different from those observed in tables 1 and 2. This new choice meets the necessity of improving the conductivity of the active layers in order to facilitate the emission under electrical pumping. To establish a reliable comparison, deposited and implanted

Table 4. MOS devices (ion-implanted).

Sample	Dose ($\times 10^{16}$ cm^{-2})	Ion energy (keV)	$[Si]_{ex}$ (at.%)	Thickness (nm)	C_{max} (pF)	N_t (cm^{-2})	Charged nc (%)
ID1	—	—	—	41.1 ± 0.3	215.51	8.456×10^{8}	—
ID2	1.2	25	9.6	46.3 ± 0.5	277.88	1.199×10^{12}	16.2
	5.0	50					
ID3	1.4	25	10.5	48.8 ± 0.2	294.78	1.509×10^{12}	19.3
	6.0	50					
ID4	1.8	25	11.7	47 ± 3	320.51	9.017×10^{11}	12.0
	7.2	50					
ID5	1.8	25	11.7	46 ± 3	308.60	4.167×10^{11}	5.7
	7.2	50					
ID6	2.0	25	12.6	50 ± 4	315.74	3.558×10^{11}	4.4
	8.3	50					

structures were prepared with similar thicknesses, about 45–50 nm. N-doped semitransparent polycrystalline silicon (poly-Si) ∼350 nm thick was deposited as a top contact layer and aluminium pads were placed to facilitate the probe connection. Before this step and only for the implanted structures, the nitride buffer was chemically etched. Even though the devices were prepared with different contact areas (see figure 3), only those with larger electrodes areas were studied (2.3×10^{-3} and 9.6×10^{-3} cm^2), since they exhibit the best signal-to-noise ratio of EL. In order to characterize the influence of the top electrode on the luminescence, transmittance spectra of the polycrystalline silicon layers were measured. To do so, poly-Si layers were deposited onto fused silica substrates and optical transmission measurements were performed with a Shimadzu UV-2101 PC spectrometer. The EL data were taken by polarizing with variable width and frequency bipolar square waves from an Agilent 8114A Pulse Generator. Time-resolved electroluminescence was detected with the photon-counting set-up described above. The EL spectra were measured by means of a Princeton Instruments 100B LN (liquid-nitrogen) cooled CCD camera and an Oriel MS257 1/4 m monochromator. Quasi-static I–V (current–voltage) and C–V (capacitance–voltage) characteristics were measured using an Agilent B1500 semiconductor device analyser.

3. Structural characterization

3.1. PECVD

Table 1 shows, apart from the nominal $[N_2O]/[SiH_4]$ ratio and the Si excess yield by XPS measurements, the thickness of as-deposited and annealed PECVD layers measured by ellipsometry. After high temperature annealing (1250 °C), the ellipsometry measurements revealed an important reduction in the layer thickness due to H desorption and atomic redistribution. This compaction has also been reported in [13]. The hydrogen comes from the decomposition of silane (SiH_4) precursor, so the densification of the layers is more evident in samples with high Si contents. XPS profiling revealed quite flat Si concentration profiles in all the SRO layers, a desirable feature for the achievement of uniform Si-nc distributions. These layers are also characterized by a relatively high concentration of N atoms incorporated from the decomposition of the N_2O precursor.

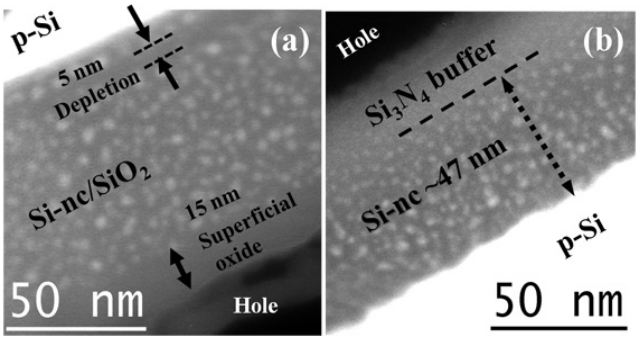

Figure 1. EFTEM profile images of sample P2 (a) and sample I3 (b).

In order to characterize the Si-nc distribution profile of PECVD samples, cross-section images were performed by EFTEM (see figure 1(a)). In good agreement with the flat Si profile observed by XPS, the Si-nc distribution is quite uniform, with a mean size of ∼3.60 nm (standard deviation of $\sigma = \pm 0.50$ nm), a density of nanocrystals of about 9.0×10^{17} cm^{-3} and an average distance between the closest nanocrystals of about 4 nm. An important result depicted in figure 1(a) is the appearance of a ∼5 nm Si-nc-free region close to the substrate, which has an important impact on device performance (as discussed hereafter). This absence of nanoparticles is attributed either to a diffusion of Si atoms to the substrate during the annealing and to the characteristic deposition instabilities at the first stages of the PECVD process. On the other hand, it is worth noting the strong oxidation of the surface (∼15 nm), which is probably induced by the high porosity of the as-deposited layers. This layer will be eliminated for device fabrication.

3.2. Ion implantation

Implanted samples were characterized in a similar way. The thickness and the Si excess of the different layers are indicated in table 2. The thickness was determined by ellipsometry and the content of Si was extracted from the XPS profiles. Similarly to the PECVD samples, a flat profile of silicon is observed in the active layer in agreement with SRIM simulations. It is remarkable the significant content of nitrogen

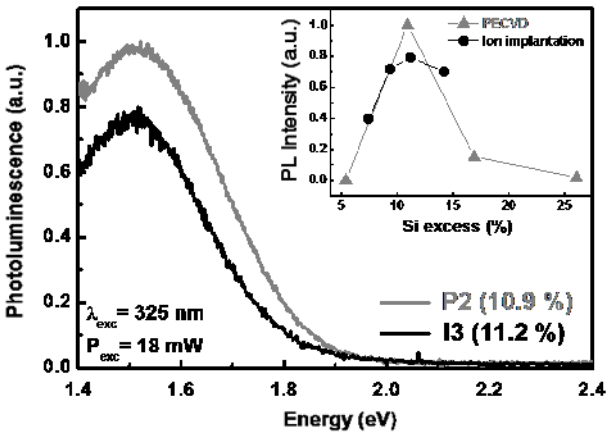

Figure 2. Photoluminescence spectra of samples P2 and I3. In the inset, the PL intensity of implanted and PECVD samples is represented as a function of the Si excess.

in the SRO layer, diffused from the buffer layer during implantation.

EFTEM images were taken in order to study the characteristics of the Si-nc distribution. Figure 1(b) shows an example of Si-nc spatial distribution. The cross-section view corresponds to sample I3. The distribution is continuous and uniform, unlike PECVD samples where a thin depletion of Si-nc was observed. An average size of ∼3.10 nm (standard deviation $\sigma = \pm 0.47$ nm) was measured with an Si-nc density of about 1.6×10^{18} cm^{-3} and an average distance between closest neighbours of ∼3 nm. Note that, in spite of the similar Si contents in samples I3 and P2, the mean Si-nc size is slightly different (∼3.10 nm in sample I3 as opposed to ∼3.60 nm in sample P2) which is, in some way, compensated by the different Si-nc densities observed. The ∼5 nm SiO_2 layer observed at the surface is a signature of oxidation by air exposure, probably induced by the implantation process. Also in this case, prior to device fabrication this layer is removed.

4. Emission properties

Figure 2 compares the PL spectrum of samples P2 and I3. The emission, placed in the range of 1.4–1.7 eV, correlates with the typical luminescence in Si-nc/SiO_2 systems. The inset shows the dependence of the PL intensity in deposited and implanted samples as a function of the Si excess. All the values were normalized to their respective layer thickness and to the most intense emission value obtained from sample P2. The plot reveals a good agreement between both PECVD and implanted samples with a maximum emission intensity found for layers with ∼11% of Si excess, i.e. samples I3 and P2. The inefficient excitation observed at low Si concentrations is related to the small size (smaller number of absorbing states) and number of grown nanocrystals. In contrast, the poor emission observed for high Si content is due to the loss of quantum confinement and the emergence of quenching effects with neighbouring nanocrystals [14, 15]. Taking into account the density of Si-nc calculated from EFTEM images, one can expect that sample I3 would exhibit a higher PL intensity. However, the emission

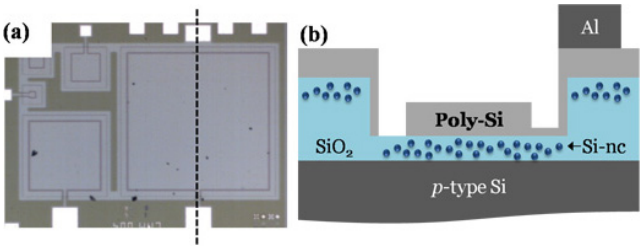

Figure 3. (a) Top-view image of fabricated MOS devices with different contact areas. (b) Cross-section view of the MOS structures. (This figure is in colour only in the electronic version)

from sample I3 is approximately 20% lower than that of sample P2, which probably suggests that the increase of the density of Si-nc is detrimental, as the interaction between neighbours and non-radiative processes is favoured, in spite of the smaller size of the Si-nc (∼3.1 nm as opposed to ∼3.6 nm in sample P2).

In order to calculate the absorption cross section of the different samples (implanted and PECVD), time-resolved measurements were performed. The PL transients were modelled by means of stretched exponential functions [16], which led, in both cases, to emission lifetimes in the range of ∼10–∼45 μs with values of β in the range of 0.60–0.70. With respect to the absorption cross sections, our calculations reveal values of σ_{abs} of the order of 10^{-16} cm^2 for both kinds of samples, in good accordance with values typically reported [17].

5. Device characterization

Metal-oxide-semiconductor structures with different active areas were fabricated by means of a standard photolithographic process. Figure 3(a) is a top-view image of the device. A basic cross-section scheme of these devices can be seen in figure 3(b). The top electrode is a 350 nm semitransparent poly-Si with an average transmittance of about 50% in the range of interest. The active layers typically have ∼45–50 nm and have been prepared with different Si contents, taking into account the results depicted in the inset of figure 2 and bearing in mind the necessity of improving the conductivity of the active layers. In order to maximize the signal-to-noise ratio of the electroluminescence trace, this work is mainly focused on devices with larger electrode areas (9.6×10^{-3} and 2.3×10^{-3} cm^2).

5.1. PECVD

Table 3 summarizes some basic characteristics of MOS structures fabricated by PECVD.

Forward–backward C–V characteristics were measured (see the example in the inset of figure 4) in order to obtain the density of trapped charge inside the SRO layer, N_t. To ensure an effective carrier injection, the voltage sweeps were adjusted for each sample taking into account its respective onset of emission and breakdown voltage (if any). The results are summarized in table 3. The trapped charge is calculated

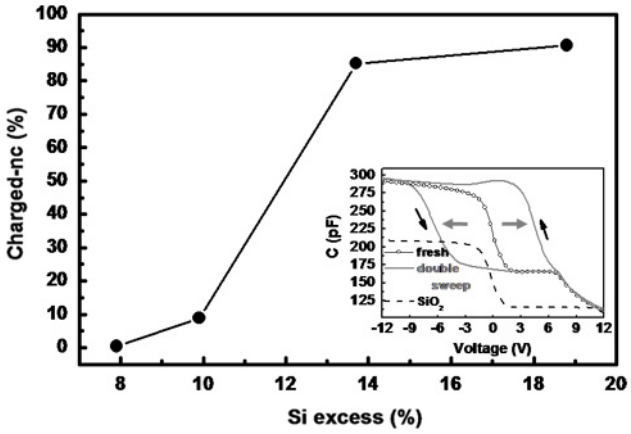

Figure 4. Variation of the ratio of charged nc as a function of the Si excess. In the inset, an example of an C–V curve is represented (device area 2.3×10^{-3}). The grey arrows indicate the flat-band voltage shift and the black ones indicate the sweep direction.

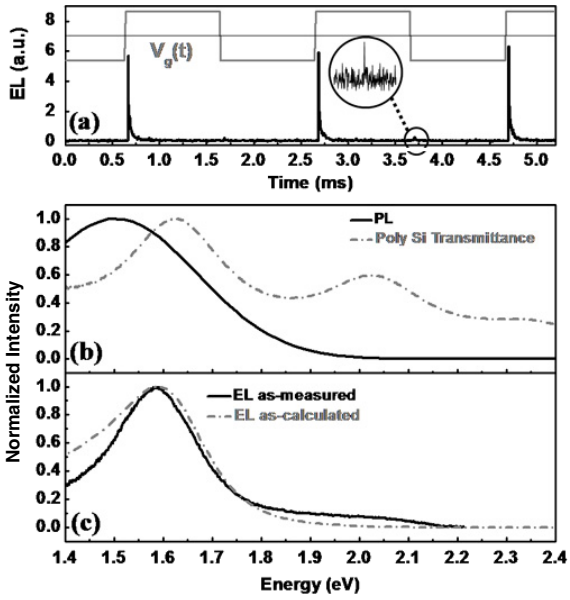

Figure 5. (a) Time-resolved electroluminescence of sample PD3 under 25 V alternate polarization. (b) The PL spectrum of layer P2 (layer without top electrode) and the poly-Si top electrode transmittance. (c) Comparison between the as-measured EL spectrum (from device PD3) and that obtained from the combination of the poly-Si transmittance and the PL spectrum given in (b).

from the shifts of the flat-band voltage, ΔV_{FB}, measured from a reference C–V curve of a fresh device:

$$N_{\mathrm{t}} = \frac{C_{\max} \Delta V_{\mathrm{FB}}}{eS} \tag{1}$$

where $C_{\max}$ represents the maximum capacitance of the structure (capacitance in accumulation regime), e is the electron charge and S is the device area. The values of N_{t} are indicated in table 3. The density of trapped charge shows a significant increase with the Si content, which is due to the concurrence of the following features: (1) the enhanced conductivity of the SRO layers and (2) the increase of the average Si-nc size that facilitates the carrier trapping.

The density of trapped charge, in combination with the Si-nc density obtained by EFTEM, leads to a rough estimation of the percentage of charged nanocrystals. This parameter is rather an upper bound to the ratio of excitable Si-nc and, in some way, can be considered as a marker of the room available to further improve the excitation efficiency, since it also indicates the ratio of non-active Si-nc. The calculation is performed under the assumption that most of the trapped charge is associated with the Si-nc, which is justified by the low value of N_{t} observed in pure oxide structures (device PD1). Nevertheless, it is also true that the addition of the Si excess causes the generation of defects and traps not observed in SiO_2 that probably leads to an overestimation of the number of active Si-nc. Figure 4 shows the results of these calculations. For low Si contents, i.e. structures PD2 and PD3, the thin zone depleted of Si-nc strongly limits the carrier injection from the substrate, leading to occupation ratios of ∼0.4% and ∼8.9%, respectively. As the Si excess further increases (up to ∼13.7%, sample PD4), there is a significant increase in the number of carriers injected from the substrate. In this case, the higher Si concentration facilitates the tunnelling from the substrate at lower voltages, leading to the highest percentages of trapped charge in devices PD4 and PD5 with values close to ∼90%. This behaviour is very similar to that observed when the tunnel oxide thickness is modified, as reported in reference [18].

In order to study the conduction mechanisms, quasi-static current–voltage characteristics were acquired under forward–backward voltage sweeps. In all the PECVD structures, the current is, in the range of interest (emission range), well fitted by Fowler–Nordheim (FN) tunnelling with injection barrier heights that decrease with the Si content: from 2.3 eV in sample PD2 (7.9%) to 0.9 eV in sample PD5 (18.8%). In accordance with this, the onset of the FN injection also exhibits significant reduction with the Si content: from 23 V in sample PD2 to 6–7 V in sample PD2.

Figure 5 summarizes the behaviour of the field-effect luminescence in PECVD structures. Figure 5(a) shows the time-resolved EL of sample PD3 under application of square wave voltages with an amplitude of 25 V, whereas figures 5(b) and (c) represent the PL and EL spectra of similarly prepared samples, respectively. The onset of the emission decreases with the Si content from ∼20 V, in structure PD2 (7.9%), to ∼6 V, in sample PD5 (18.8%), as depicted in figure 6(a). It should be noted the good accordance between the onsets of emission and FN injection, which clearly links the field-effect emission of PECVD samples to this injection mechanism. The field-effect mechanism entails the sequential injection of electrons and holes from the substrate, in a process assisted by the Coulomb field attraction from the previously stored carriers. Note that, during the second carrier injection, a sizeable percentage of the trapped charge tunnels back to the substrate and therefore the achievement of an efficient emission depends on both the retention time of the first carrier injected and the tunnelling time of the incoming second carrier. Due to the lower barrier for electrons, the migration of the stored charge is more marked when holes are injected into electron-charged Si-nc, which results in a weaker emission compared to the

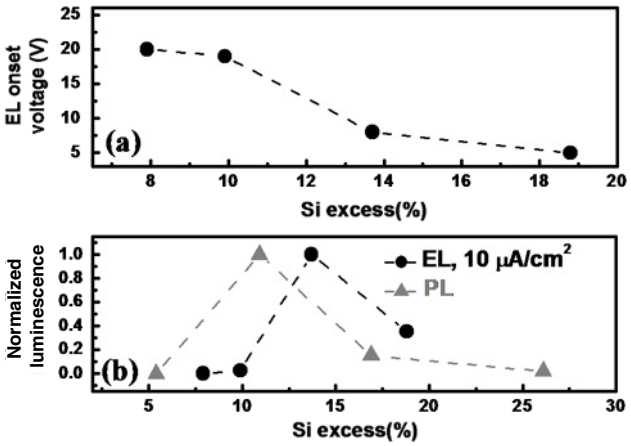

Figure 6. (a) Variation of the EL onset voltage of PECVD structures with the Si excess. (b) Evolution of the PL and EL intensities with the Si content.

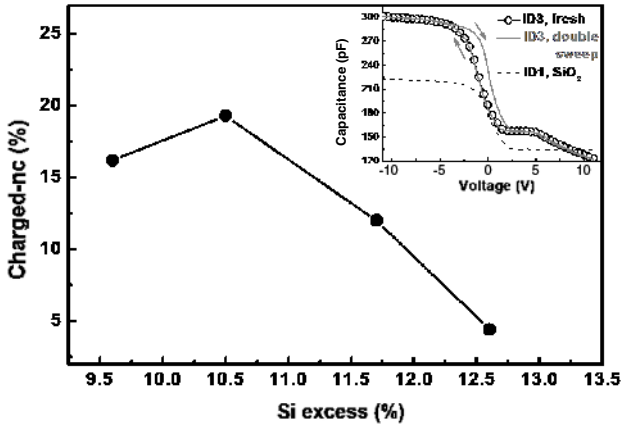

Figure 7. Ratio of charged nc as a function of the Si excess. The inset represents an example of C–V curves obtained from sample ID3 (device area 2.3×10^{-3}). The arrows indicate the sweep direction.

case of electron injection into hole-charged nanocrystals [22]. This behaviour is clearly seen in figure 5(a), where the EL intensity of the peaks differs by approximately one order of magnitude. The hole-triggered peak is slightly faster in duration, even though the difference with the peak associated with the electron injection into hole-charged Si-nc does not appear to be significant. In any case, both transients are faster than those observed under optical excitation. The emission decays are well fitted by stretched exponential functions with time constants slightly shorter than in the case of PL; ranging from $\sim$5 to $\sim$20 μs, with $\beta \sim 0.5$. Operating under a field-effect mechanism, the absorption cross sections are of the order of $\sim 10^{-11}$ cm^2, approximately three orders of magnitude larger than values usually reported under DC excitation [19]. Some authors have pointed out [20, 21] that typically reported values of $\sim 10^{-14}$ cm^2 should be interpreted as a lower bound, since leakage currents not contributing to the emission are unavoidably included in the calculations. In addition, in reference [20], Carreras *et al* reported a theoretical estimate of the field-effect absorption cross section of about 10^{-12} cm^2. In the light of this, our results should be considered as the consequence of a strong reduction of the leakage current (thanks to the AC polarization) that leads to a better profit of the injected charge. The comparison of PL and EL spectra reveals modulation of the emission due to interference phenomena inside the poly-Si electrode. This effect is clearly seen if one compares the measured EL spectrum with the one obtained by combining the PL emission and the electrode transmittance represented in 5(b). The good match between both spectra (see figure 5(c)) underlines the relevant role played by the top contact on the emission properties.

Figure 6(b) shows the EL and PL intensities as a function of the Si content. The EL corresponds to a fixed current density of ~ 10 μA cm^{-2}. In accordance with the quantum confinement theory (QCT), PL and EL intensities exhibit similar behaviours, even though the EL intensity peaks at higher Si contents than in the case of the emission under optical pumping, $\sim$13.7% versus $\sim$11.2%. This difference is due to the fact that, under electrical pumping, an optimum emission requires an additional amount of Si in order to improve carrier injection. The device breakdown also depends on the Si excess, since it is related to the current level through the device. The samples with large Si contents, PD5 and PD6, break down at about 14 V and 22 V respectively, whereas the samples with low Si concentrations do not show an observable breakdown, even for voltages higher than 30 V.

5.2. Ion implantation

The characteristics of the different devices fabricated by ion implantation are presented in table 4. C–V characteristics were measured in order to obtain the density of trapped charge, N_t. The inset of figure 7 shows a typical C–V curve of implanted devices. In general, the capacitance hysteresis is characterized by a sizeable trapping of electrons that is related to an easier carrier injection (if compared with PECVD), as demonstrated below. The density of trapped charge is calculated from the capacitance hysteresis cycle with a similar procedure than in the case of PECVD samples. The calculations reveal a maximum value of N_t in structures with low Si concentrations. In those structures (ID2 and ID3), typical densities of ~ 1.0–1.5×10^{12} cm^{-2} are observed that represent percentages of charged nanocrystals of about 16–19%. As the Si concentration increases, there is a progressive reduction of trapped charge (see figure 7) probably related to the increased conductivity and the subsequent carrier migration. The trapped charge decreases down to $\sim 4 \times 10^{11}$ cm^{-2} in structure ID6, which corresponds to an occupation ratio of $\sim$4.4%. In order to study the conduction mechanisms, I–V characteristics were acquired. The current is, in general, higher than in the case of PECVD structures due to the continuous and uniform Si-nc distribution. The I–V curves are well fitted by FN expressions with low injection barriers (if compared with PECVD): about 0.2 eV. The onset of the FN regime is placed in the range of $\sim$2–3 V. The analysis of the EL is represented in figure 8: (a) shows the time-resolved EL of structure ID4 under a 9 V square wave voltage and (b) depicts the EL spectrum of each device. Time-resolved measurements reveal that, apart from the field-effect transients, there is a significant DC contribution during

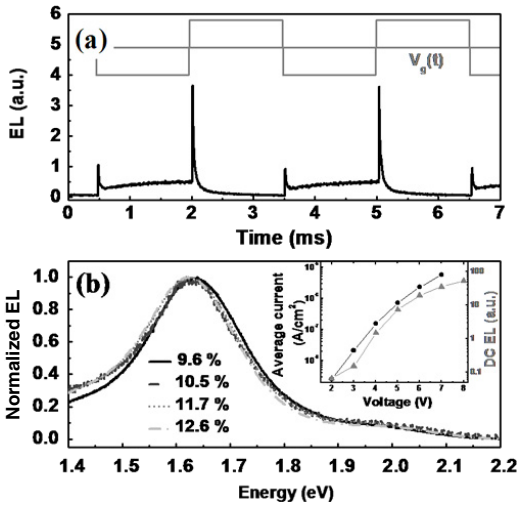

Figure 8. (a) Time-resolved EL of sample ID4 under 9 V square waves. (b) EL spectra of the different implanted structures. In the inset, the average current and the DC EL emission of sample ID6 are represented as functions of the gate voltage.

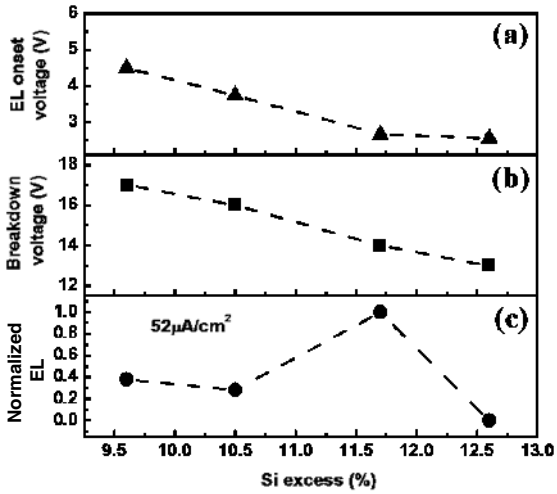

Figure 9. (a) Variation of the onset voltage of implanted structures. (b) Breakdown voltage of the same set of samples as a function of the Si content. (c) Dependence of the EL intensity on the Si excess.

the negative half-cycle of the driving signal. This component is approximately one order of magnitude larger than the field-effect luminescence (for driving signals of ∼1 kHz) and is likely related to the continuous Si-nc distribution observed in implanted structures. The inset of figure 8(b) compares the average current through the SRO layer with the intensity of the DC EL; both magnitudes as a function of the driving voltage. The good accordance between both curves suggests that impact ionization is the mechanism responsible for the DC emission. Bipolar injection from opposite electrodes could also be possible and could perfectly explain the DC component observed, since it is only present during the negative half-cycle of the gate bias. However, this possibility is less probable due to the thickness of the layers.

The transients of the DC contribution are approximately one order of magnitude longer than those of the field-effect emission. Decay times of up to 0.7 ms (structure ID6) with $\beta \sim 0.5$ were observed. These lifetimes were extracted by modelling the de-excitation at the rise edge of the gate bias with two exponentials: the first one corresponding to the fast AC transient and the second one associated with the continuous emission. The value of $\sigma_{\mathrm{abs}}^{\mathrm{EL}}$ was found around 3×10^{-14} cm^2, in agreement with values usually reported from Si-nc-based devices under DC polarization [19].

With respect to the field-effect transients, it is clearly seen in figure 8(a) that the electron-triggered emission is larger in intensity than that observed when holes are injected into electron-charged Si-nc, even though the difference between these two peaks is not as significant as in deposited structures (due to some extent to the higher conductivity of the layer). The decay times of both peaks are very similar with values in the range of ∼20–30 μs. These decays were extracted from stretched exponential fits with typical β of about 0.5. Absorption cross sections of about 2×10^{-12} cm^2 were obtained, approximately two orders of magnitude higher than that for the DC emission. This difference suggests that the field-effect mechanism takes best profit of the injected charge in comparison to the impact ionization mechanism. Note that in PECVD samples the value of $\sigma_{\mathrm{abs}}^{\mathrm{EL}}$ is one order of magnitude higher, which is attributed to their relatively low operation currents.

Figure 8(b) shows the EL spectra of the different implanted devices under 9 V square wave voltages. The apparent immobility of the emission peak with the Si content is related to the modulation induced by the transmittance of the poly-Si layer, as discussed above. Figure 9(a) represents the EL onset voltage as a function of the Si excess. The addition of Si favours the carrier injection and shifts the onset voltage to lower values. Nevertheless, this leads to higher current flows that unavoidably lead to lower breakdown voltages, as shown in figure 9(b). Note that also in the case of implanted MOSLEDs there is a good agreement between the onsets of emission and FN tunnelling. The integrated EL was studied in the different structures for a given current flow of ∼52 μA cm^{-2} (see figure 9(b)). The dependence of the emission on the Si excess is very similar to the results presented in the inset of figure 2, and is in good agreement with the QCT. The maximum emission is observed in device ID5 (11.7% of Si excess).

6. LED performances

In order to study the suitability of PECVD and implanted devices as candidates for an Si-nanocrystal-based LED implementation, we compare in this section the best operational performances of these structures. Figure 10(a) shows the response of the field-effect luminescence of samples ID5 and PD3 (with similar Si contents) to different driving frequencies. First, the curves show that, as the integration time is held constant, enhancement of the EL signal is initially observed due to the increasing number of integrated cycles [22]. The EL intensity peaks at a frequency that is determined by both the tunnelling dynamics and recombination

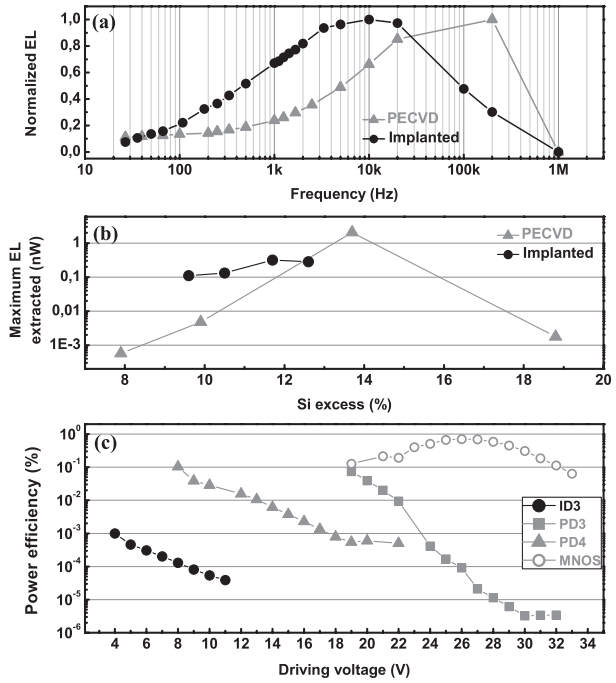

Figure 10. (a) EL response of samples ID5 and PD3 versus the driving frequency. (b) Maximum output power extracted from the different samples. (c) Variation of the emission power efficiency with the driving voltage.

times. As shown in the plot, the shorter transient times observed in PECVD structures allow a faster modulation of the emission compared with implanted samples. Figure 10(b) compares the maximum EL intensity achievable for PECVD and implanted samples. To obtain this value, the devices were biased at its optimum frequency (see figure 10(a)) with amplitudes close to the breakdown voltage (if any). Implanted devices exhibit typical emission powers of ∼0.1–0.3 nW. The slight increase observed with the Si content is related to the higher conductivity of the layers and, consequently, mostly due to larger contributions of the DC mechanism. Note that the quantum confinement modulation of the emission seen in figure 10(c) is not observed, which is due to the fact that EL intensities were calculated at different pump fluxes (the maximum before breakdown). With respect to PECVD structures, the most intense emission is observed in sample PD4 with a maximum output power of ∼2 nW (higher than those in implanted samples) that contrasts with the low values of the rest of the deposited structures that exhibit maximum output powers lower than 0.01 nW. By comparing these results with the ratio of charged nanocrystals represented in figure 4, it becomes clear that, for low Si contents (samples PD2 and PD3), the poor emission obtained is due to a deficient carrier injection into the Si-nc, as only a small part of the Si-nc distribution can be excited (∼0.4% and ∼8.9%, respectively). In contrast, for samples PD4 and PD5 the ratio of excitable Si-nc is remarkably higher (∼90%), but only in the first case intense emission is observed. The weak emission of sample PD5 is, in contrast to samples PD2 and PD3, associated with the loss of quantum confinement and to the emergence of carrier migration phenomena. Figure 10(c) compares the power efficiency of different deposited and implanted samples to the values obtained from a reference device, with an MNOS (metal nitride oxide semiconductor) configuration that has been recently reported as a high-efficiency structure [23]. A thin buffer of pure Si_3N_4 (∼15 nm) is deposited onto the SRO in order to limit the device leakage current. More details about this kind of structure can be found in reference [23]. The values depicted in figure 10(c) are calculated by adjusting the gate voltage to its optimum frequency and under the assumption that the emission pattern of these devices is approximately Lambertian. The implanted samples present maximum values of efficiency of $\sim 10^{-3}$ % that rapidly decrease with the applied voltage as the increasing power consumption is not compensated by the gain in the output power. Thanks to the low current levels observed in PECVD samples, their values of power efficiency are typically two orders of magnitude higher than that observed in implanted structures, up to ∼0.1%. Also in this case, a fast reduction of the efficiency with the applied voltage is observed, mostly due to the strong increase of the FN current at higher fields. In the case of the MNOS structure, the nitride buffer reduces the device leakage current leading to a better profit of the injected charge that translates into power efficiencies of about 1% and output emission powers of ∼10 nW. It is worth noting the slow variation of the power efficiency with the gate bias in MNOS structures that is attributed to the increase of the FN onset [23].

Based on these results, it is clear that, in order to achieve efficient devices, the fabrication of discontinuous Si-nc distributions appears to be beneficial, as it reduces the device power consumption. On the other hand, if we take into account the ratios of charged nanocrystals represented in figures 4 and 7, it is also clear that, apart from the reduction of the power consumption, the power efficiency can be improved by increasing the number of excited Si-nc. This should be done by accurately controlling the amount of defects and the size and position of the Si-nc distribution. In the light of our results, the combination of these two factors could enhance the power efficiency of Si-nc-based MOS devices up to ∼1–10% with typical powers in the range of ∼10–20 nW.

Implanted and PECVD structures were submitted to accelerated ageing for more than 24 h of continuous operation under application of 13 V and 30 V square waves, respectively, at a frequency of 1 kHz. Figure 11 shows the degradation of the emission for samples PD4 and ID6. The plot shows that sample ID6 exhibits an emission degradation rate of about 45% that contrasts with the lower value observed in sample PD4, about 20%. This difference correlates with the respective current levels observed in I–V characteristics. Both curves are well fitted by a logarithmic function within the experimental timescale [24], resulting in estimated lifetimes of at least several months.

7. Conclusions

The luminescence of Si-nc/SiO_2 layers fabricated by PECVD and ion implantation has been thoroughly studied under optical and electrical excitation. The results have been correlated with an exhaustive characterization of the structural and electrical

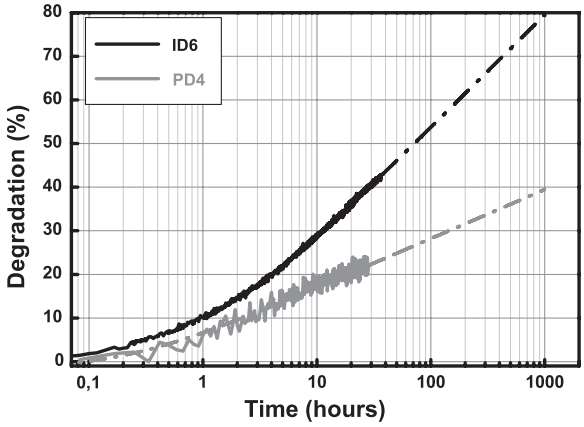

Figure 11. Degradation of the emission in structures ID6 and PD4 as a function of the operation time.

properties. First, XPS and EFTEM measurements revealed that, in spite of the almost flat profile of Si excess, PECVD layers exhibited a ∼5 nm Si-nc free region, attributed either to the diffusion of Si to the substrate or to the instabilities at the first stages of the deposition process. In implanted layers, the profile of added Si is also relatively flat (XPS) and translates into a uniform and continuous Si-nc distribution (EFTEM), which clearly underlines the suitability of the implantation process. We have also shown that, for similar Si contents, the average sizes of the Si-nc obtained by ion implantation are smaller than those observed in deposited layers, which leads to a higher Si-nc density and shorter interdot (interaction range) distances. The PL emission showed a good agreement between PECVD and implanted samples with maximum intensities of emission for layers with ∼11% of Si excess. In both cases, the absorption cross sections are of the order of 10^{-16} cm^2.

EL measurements have been performed by polarizing with bipolar and monopolar square wave voltages. The EL spectra of implanted and PECVD structures reveal typical emission from Si-nc/SiO_2 systems that correlates with PL results. A strong modulation of the spectral shape and peak position is observed due to interference phenomena in the poly-Si top contact. The time-resolved EL revealed both AC and DC emission from implanted samples, in contrast to the measurements carried out in PECVD devices, where only transient emission was observed. The absence of emission under constant electrical excitation in the deposited layers is due to the discontinuous Si-nc distribution that hinders the DC flow through the structure. Moreover, this current reduction results in onset and breakdown voltages remarkably higher than in the case of implanted samples. The absorption cross sections of the implanted AC and DC emission are of the order of $\sim 10^{-12}$ and $\sim 10^{-14}$ cm^2, several orders of magnitude higher than those values obtained by photoexcitation. In the case of PECVD structures the value of σ_{abs}^{EL} is approximately $\sim 10^{-11}$ cm^2. The maximum of the EL intensity is observed in implanted and PECVD structures with Si contents between 11–13%, apparently higher than that under optical excitation. We have also shown the limited frequency response of gate-biased Si-nc-based MOS structures, attributed to the characteristic radiative lifetimes of the Si nanoparticles. The maximum EL intensities obtained are ∼0.3 nW for implanted devices and ∼2 nW for PECVD. The efficiency of the implanted devices is of about 10^{-3}%, two orders of magnitude lower than the one obtained for PECVD structures, 0.1%. This result tells us that, in terms of efficiency, a continuous distribution of Si-nc appears to be detrimental.

In order to evaluate the room available to further enhance the emission capabilities in these LEDs, a rough estimation of the electrically active Si-nc (percentage of charged nanocrystals) has been performed. We have shown that most of the structures (both PECVD and implanted) exhibit poor percentages of charged nanocrystals. With an accurate control of the amount of defects and the size and position of the Si-nc it could be possible to increase the excitation efficiency. Thus the optical output power could be enhanced up to ∼20 nW, with typical power efficiencies in the range of 1–10%.

Finally, accelerated ageing studies reveal stronger degradation of the emission in implanted devices, which is attributed to their higher current levels in comparison to PECVD devices.

Acknowledgments

This work has been partially supported by the project MILES-SILUZ: TEC2006-13907/MIC, financed by the Spanish Ministry of Education and Science. AM and JB acknowledge the grants received from CONACyT-FC and CSIC (I3P), respectively. MP acknowledges Dr O Jambois, R Rodríguez-Trujillo, Y Berencén, Drs J Arbiol and L Calvo.

References

[1] Carreras J, Arbiol J, Garrido B, Bonafos C and Montserrat J 2008 Direct modulation of electroluminescence from silicon nanocrystals beyond radiative recombination rates *Appl. Phys. Lett.* **92** 091103

[2] Jaiswal S L, Simpson J T, Withrow S P, White C W and Norris P M 2003 Design of a nanoscale silicon laser *Appl. Phys.* A **77** 57–61

[3] Jalali B and Fathpour S 2006 Silicon photonics *J. Lightwave Technol.* **24** 4600–15

[4] Redding B, Creazzo T, Marchena E, Shouyuan S and Prather D W 2008 Design, fabrication, and characterization of a 1D microcavity for enhanced luminescence from silicon nanocrystals *GFP: 5th IEEE Int. Conf. on Group IV Photonics* 2008 pp 329–31

[5] Rong H S, Jones R, Liu A S, Cohen O, Hak D, Fang A and Paniccia M 2005 A continuous-wave Raman silicon laser *Nature* **433** 725–8

[6] De la Torre J *et al* 2003 Optical properties of silicon nanocrystal LEDs *Physica* E **16** 326–30

[7] DiMaria D J, Kirtley J R, Pakulis E J, Dong D W, Kuan T S, Pesavento F L, Theis T N, Cutro J A and Brorson S D 1984 Electroluminescence studies in silicon dioxide films containing tiny silicon islands *J. Appl. Phys.* **56** 401–16

[8] Irrera A *et al* 2005 Correlation between electroluminescence and structural properties of Si nanoclusters *Opt. Mater.* **27** 1031–40

[9] Luterova K, Pelant I, Valenta J, Rehspringer J L, Muller D, Grob J J, Dian J and Honerlage B 2000 Red electroluminescence in Si^+-implanted sol–gel-derived SiO_2 films *Appl. Phys. Lett.* **77** 2952–4

[10] Peralvarez M, Garcia C, Lopez M, Garrido B, Barreto J, Dominguez C and Rodriguez J A 2006 Field effect luminescence from Si nanocrystals obtained by plasma-enhanced chemical vapor deposition *Appl. Phys. Lett.* **89** 3

[11] Walters R J, Bourianoff G I and Atwater H A 2005 Field-effect electroluminescence in silicon nanocrystals *Nat. Mater.* **4** 143–6

[12] Ziegler J F 2004 SRIM-2003 *Nucl. Instrum. Methods Phys. Res.* B **219** 1027–36

[13] Hernandez S, Martinez A, Pellegrino P, Lebour Y, Garrido B, Jordana E and Fedeli J M 2008 Silicon nanocluster crystallization in SiO_x films studied by Raman scattering *J. Appl. Phys.* **104** 044304

[14] Garrido B, Lopez M, Garcia C, Perez-Rodriguez A and Morante J R 2002 Influence of average size and interface passivation on the spectral emission of Si nanocrystals embedded in SiO_2 *J. Appl. Phys.* **91** 798–807

[15] Belyakov V A, Burdov V A, Lockwood R and Meldrum A 2008 Silicon nanocrystals: fundamental theory and implications for stimulated emission *Adv. Opt. Technol.* **2008** 279502

[16] Linnros J, Lalic N, Galeckas A and Grivickas V 1999 Analysis of the stretched exponential photoluminescence decay from nanometer-sized silicon crystals in SiO_2 *J. Appl. Phys.* **86** 6128–34

[17] Garcia C, Garrido B, Pellegrino P, Ferre R, Moreno J A, Morante J R, Pavesi L and Cazzanelli M 2003 Size dependence of lifetime and absorption cross section of Si nanocrystals embedded in SiO_2 *Appl. Phys. Lett.* **82** 1595–7

[18] Garrido B, Cheylan S, Gonzalez-Varona O, Perez-Rodriguez A and Morante J R 2003 The effect of additional oxidation on the memory characteristics of metal-oxide-semiconductor capacitors with Si nanocrystals *Appl. Phys. Lett.* **82** 4818–20

[19] Irrera A, Pacifici D, Miritello M, Franzo G, Priolo F, Iacona F, Sanfilippo D, Di Stefano G and Fallica P G 2002 Excitation and de-excitation properties of silicon quantum dots under electrical pumping *Appl. Phys. Lett.* **81** 1866–8

[20] Carreras J and Garrido B 2008 Modeling direct modulation dynamics in silicon nanocrystal light emitting transistors *5th IEEE Int. Conf. on Group IV Photonics 2008* pp 326–8

[21] Valenta J, Lalic N and Linnros J 2004 Electroluminescence of single silicon nanocrystals *Appl. Phys. Lett.* **84** 1459–61

[22] Walters R J, Carreras J, Feng T, Bell L D and Atwater H A 2006 Silicon nanocrystal field-effect light-emitting devices *IEEE J. Sel. Top. Quantum Electron.* **12** 1647–56

[23] Peralvarez M, Carreras J, Barreto J, Morales A, Dominguez C and Garrido B 2008 Efficiency and reliability enhancement of silicon nanocrystal field-effect luminescence from nitride-oxide gate stacks *Appl. Phys. Lett.* **92** 241104

[24] Cui Z, Liou J J and Yue Y 2003 A new extrapolation method for long-term degradation prediction of deep-submicron MOSFETs *IEEE Trans. Electron Devices* **50** 1398–401